

Overcoming the bottleneck for quantum computations of complex nanophotonic structures: Purcell and Förster resonant energy transfer calculations using a rigorous mode-hybridization method

Gilles Rosolen^{✉*} and Bjorn Maes

*Micro and Nanophotonic Materials Group, Research Institute for Materials Science and Engineering,
University of Mons, 7000 Mons, Belgium*

Parry Yu Chen and Yonatan Sivan[✉]

School of Electrical and Computer Engineering, Ben-Gurion University, 635 Beersheba, Israel



(Received 5 December 2019; revised manuscript received 10 February 2020; accepted 12 March 2020;
published 1 April 2020)

A calculation of the photonic Green's tensor of a structure is at the heart of many photonic problems, but for nontrivial nanostructures, it is typically a prohibitively time-consuming task. Recently, a general normal-mode expansion (GENOME) was implemented to construct the Green's tensor from eigenpermittivity modes. Here, we employ GENOME to study the response of a cluster of nanoparticles. To this end, we use the rigorous mode-hybridization theory derived earlier by D. J. Bergman [Phys. Rev. B **19**, 2359 (1979)], which constructs the Green's tensor of a cluster of nanoparticles from the sole knowledge of the modes of the isolated constituent. The method is applied to a scatterer with a nontrivial shape (namely, a pair of elliptical wires) within a fully electrodynamic setting and for the computation of the Purcell enhancement and Förster resonant energy transfer rate enhancement, showing good agreement with direct simulations. The procedure is general, is trivial to implement using standard electromagnetic software, and holds for arbitrary shapes and number of scatterers forming the cluster. Moreover, it is orders of magnitude faster than conventional direct simulations for applications requiring the spatial variation of the Green's tensor, promising wide use in quantum technologies, free-electron light sources, and heat transfer, among others.

DOI: [10.1103/PhysRevB.101.155401](https://doi.org/10.1103/PhysRevB.101.155401)

I. INTRODUCTION

It is well known that the emission properties of a quantum emitter (QE) depend on its electromagnetic (EM) environment, i.e., on the Green's tensor. For instance, the Purcell enhancement, which quantifies the modification of the decay rate of a QE through the EM environment [1], is determined by the imaginary part of the Green's tensor [2]. Enhancing or inhibiting the Purcell enhancement has been under extensive research for its potential applications for single-photon sources [3], quantum sources [4], spectroscopy [5], and so on.

Resonant energy transfer (RET) is another phenomenon strongly influenced by the Green's tensor. RET is the exchange of energy between two QEs, a donor and an acceptor, and depends on the total complex Green's tensor [2,6]. However, for a long time, it was thought that enhancing the RET comes down to enhancing the Purcell enhancement (i.e., considering only the imaginary part of the Green's tensor), which led to contradictory experiments, sometimes enhancing [7–10] and sometimes suppressing [11–13] the RET rate in the vicinity of photonic cavities or nanoparticles. Recently, it was shown that Purcell enhancement and RET are uncorrelated [14,15], implying that both the real and imaginary parts of the Green's tensor need to be computed.

Two well-known mechanisms are associated with migration of energy, depending on the distance R between the QEs [16,17]: one in the near field with a rate varying with an R^{-6} dependence, a radiationless transfer called the Förster resonant energy transfer (FRET), and a radiative transfer in the far field with a rate varying with an R^{-2} dependence. FRET is unique in generating fluorescence signals sensitive to molecular conformation, association, and separation and has been applied in molecular imaging techniques [18], quantum-based biosensors [19], and photovoltaic devices [20]. It is enhanced significantly close to nanostructures such as a graphene sheet [21] and spherical nanoparticles [22] and around a dimer of (i.e., two) metallic spherical particles [23]. Nevertheless, the challenge remains to determine the Green's tensor of complex, arbitrary, inhomogeneous, dispersive, and absorbing environments, either numerically or analytically. This problem limits the FRET rate investigations, with researchers typically resorting to effective models [24].

The spatial variation of the Green's tensor is known analytically for uniform media and for simple geometries. More complex structures are generally studied by direct simulation using software based on, e.g., the finite-element method [25,26] or the finite-difference time-domain method [27], to cite some of the well-known techniques. However, the computational cost is large, as repetitive simulations are necessary, because different polarizations and positions of the source are required. Much faster and more insightful techniques resort to

*gilles.rosolen@umons.ac.be

an expansion of the modes of the resonator. Once the modes are known, this allows for a fast resolution of the total spatial variation of the Green's tensor, and often, physical intuition can be gained, e.g., from the study of one or two dominant modes.

For nonconservative open systems, i.e., lossy and radiative resonators, *eigenfrequency modes* are currently widely used, leading to the *quasinormal* modes (also known as resonant states) [28–30]. Eigenfrequency modal expansions were used for the study of various important physical problems like the asymmetry of the line shape of plasmonic cavities [28], for refractive index sensing [31], for second quantization of nanocavities [32], and for the derivation of scattering matrices of complex nanocavities [33], to name a few. However, this approach is made complicated by the incompleteness of the mode set outside of the scatterers, by the need to compute them via a nonlinear eigenvalue equation, by their exponential growth in space and their nonorthogonal nature [28], by the occurrence of a large number of modes that reside in the artificial perfectly matched layer, etc. (see the detailed discussion in Ref. [34]). Intensive work of various groups has provided satisfactory solutions for these problems [30,35–39]; however, correct implementation of these solutions requires significant expertise.

In contrast to the quasinormal modes, an alternative class of *normal* modes that does not suffer from any of the above problems consists of *eigenpermittivity modes*. Indeed, in contrast to frequency eigenvalues, which are a *global* property of the system, the permittivity eigenvalue pertains only to a scattering element (or an inclusion) which spans a finite portion of space. As a result, the permittivity modes decay (rather than grow) exponentially in space (away from the scatterer), and thus, they enjoy a trivial normalization; they are orthogonal and seem to form a complete set [34,40,41]. Further, they are simple to compute since they are solutions of a linear eigenvalue problem [34]. This approach was first derived in the 1970s by Bergman [40,42] *under the quasistatic approximation*, with similar methods having been developed independently by others [41,43]. These modes have already proven useful for the computation of effective medium parameters, bounds on them, and associated sum rules [44,45] and scattering bounds of particles [46], as well as for the study of a wide variety of electromagnetic systems such as spasers [47], self-similar nanoparticle chains [48], disordered media [49], and additional effects such as coherent control [50] and second-harmonic generation [49,51,52], to name a few. The modes were computed either analytically for simple shapes [40–42,48,52,53], numerically [47,49,50], or asymptotically [54,55].

Extensions of the eigenpermittivity formulation beyond the quasistatic approximation are relatively rare. The spatial variation of modes of simple shapes like a slab [56], a wire [34,52], a sphere [40,57], and a coated sphere [58] is known, such that the differential eigenvalue problem reduces to a complex root search problem. These can be solved using reliable algorithms (see, e.g., Ref. [59]). More complicated scatterer systems require dedicated numerical computations [60–62], a challenge that significantly limited the popularity of eigenpermittivity methods. This limitation was recently removed by Chen *et al.*, who have applied the eigenpermittivity

expansion for the computation of electromagnetic fields and the associated Green's tensor of open and lossy electromagnetic systems for general nanoparticle configurations using a commercial software (COMSOL MULTIPHYSICS) [34]; in this work, the approach was coined as a generalized normal-mode expansion (GENOME). In comparison to expansions based on quasinormal modes, GENOME is trivial to implement in commercial software and converges with high accuracy.

Here, we develop another asset of GENOME in comparison with quasinormal modes: the possibility to derive the spatial Green's tensor of a *cluster* of scatterers (i.e., an assembly of N nontouching scatterers) from the knowledge of the modes of its constituents, without further mode calculations. This rigorous hybridization procedure was suggested originally by Bergman [42]. It may be regarded as a generalization to Maxwell's equations of the procedure employed for the calculation of molecular orbital calculations, an approach known as linear combination of atomic orbitals [63,64]. It was already applied for the computation of the response of a dimer (i.e., an assembly of two nontouching particles) from the modes of a monomer (i.e., one particle) under the quasistatic approximation [42,64–66], as well as for the computation of the response of a periodic array of small spheres [42,45]. In a recent paper, the full electrodynamic hybridization procedure was applied to the study of the scattered field of a simple configuration (namely, a dimer of identical spheres) and to the detailed study of the modal interplay in that system [67]. We, on the other hand, formulate a general rigorous hybridization procedure and apply it to nontrivial shapes, giving direct access to the Green's tensor, required in many classical and quantum photonic problems. We focus on the significant computational advantages of this approach and demonstrate the strength of our approach by computing Purcell and FRET maps for the structures we studied, providing physical insights. Our hybridization procedure also bears similarities to multiple-scattering formulations. These derive the scattering from a cluster or lattice by propagating among constituents with known scattering properties (e.g., using the addition theorem). By diagonalizing, modes can also be obtained [68,69]. However, multiple scattering formulations typically use the multipole basis to express fields in the vicinity of each constituent, while our hybridization method directly transforms constituent modes into cluster modes without any intermediate steps.

GENOME possesses a number of properties which allow this hybridization procedure to succeed. First, the modes form a discrete yet complete basis set within the inclusion, so the modes of each constituent are capable of representing any arbitrary field [40]. GENOME is based on the Lippmann-Schwinger equation, which is then able to obtain the correct field everywhere from this discrete basis, even though the domain is open and infinite. This allows the multiple-scattering interactions between modes of different constituents to be accounted for rigorously. Finally, since modes of the cluster and its constituents are defined by the same operator, the resulting matrix eigenvalue problem is linear. In contrast, a similar procedure would be difficult to implement for quasinormal modes, which ordinarily require a continuum of modes associated with the infinite background to ensure correct interaction between different constituents. Furthermore,

quasinormal modes of the cluster and constituents have different operators, which would lead to a nonlinear matrix eigenvalue problem.

The implementation of the rigorous hybridization method described below constitutes a rigorous generalization of the approximate quasistatic hybridization technique developed in the context of nanoplasmonics [70,71] by Prodan, Nordlander, and coworkers, while it also generalizes the previous works on eigenpermittivity modes beyond the quasistatic approximation. Our method is accurate, as validated by comparing with rigorous direct simulations and very simple to implement. Moreover, it is faster by orders of magnitude than direct simulations for problems requiring the spatial variation of the Green's tensor, such as Purcell and FRET rate enhancement calculations, as well as for geometry optimizations. In our case, we consider a dimer of ellipsoidal rods, but the method is general for any particle shape and any number of particles. The obtained dimer modes are used to calculate Purcell and FRET rate enhancements in the context of GENOME (and modal expansions, in general). Finally, our results confirm that the FRET rate enhancement is uncorrelated to the Purcell enhancement, making the real part of the Green's tensor essential.

Our rigorous hybridization method is derived in Sec. II, the implementation and comparison with direct simulation are successfully demonstrated in Sec. III, and Sec. IV summarizes our work and discusses several potential future steps.

II. RIGOROUS HYBRIDIZATION METHOD

We describe the simple and efficient procedure to generate the eigenmodes of the cluster by reusing the known eigenmodes of its individual constituents. It bears many similarities to other expansion-based solutions. It begins by inserting the expansion into the governing eigenvalue equation. Then, an orthonormal projection onto the constituent modes is used to produce a linear system of equations, to be solved for the solution. No additional simulation is necessary, requiring only the evaluation of overlap integrals generated during projection.

The governing eigenmode equation of the nanoparticle cluster can be expressed in integral form from the vector Helmholtz equation [34]. It may also be regarded as an eigenmode of the Lippmann-Schwinger equation for electromagnetism,

$$s_m \mathbf{E}_m(\mathbf{r}) = k^2 \int \bar{\bar{G}}_0(\mathbf{r}, \mathbf{r}') \theta(\mathbf{r}') \mathbf{E}_m(\mathbf{r}') d\mathbf{r}', \quad (1)$$

where $\bar{\bar{G}}_0(\mathbf{r}, \mathbf{r}')$ is the free-space Green's tensor [2], $k = \omega/c$ is the light wave vector, and $\mathbf{E}_m(\mathbf{r})$ is the electric field profile of the eigenmode m with eigenvalue s_m . It is related to the eigenpermittivity ε_m by $s_m = \varepsilon_b / (\varepsilon_b - \varepsilon_m)$, where ε_b is the background permittivity [34]. The Heaviside-type function $\theta(\mathbf{r})$ describes the geometry. It is 0 in the background and 1 in the interior of the cluster. It is a sum of disjoint geometry functions of the constituents,

$$\theta(\mathbf{r}) = \sum_a \tilde{\theta}_a(\mathbf{r}), \quad (2)$$

where a numbers the constituents and $\tilde{\theta}_a(\mathbf{r})$ is nonzero only inside inclusion a and zero elsewhere. By virtue of $\theta(\mathbf{r})$, the

left-hand side (LHS) of (1) is the field everywhere obtained from an integral defined over only the interior.

We now define the eigenmodes of each constituent; they obey an equation with a form identical to that of the cluster modes defined in Eq. (1),

$$\tilde{s}_{a,\mu} \tilde{\mathbf{E}}_{a,\mu}(\mathbf{r}) = k^2 \int \bar{\bar{G}}_0(\mathbf{r}, \mathbf{r}') \tilde{\theta}_a(\mathbf{r}') \tilde{\mathbf{E}}_{a,\mu}(\mathbf{r}') d\mathbf{r}', \quad (3)$$

but where μ is the μ th mode of constituent a . We have affixed tildes for quantities specific to the constituent modes. Owing to completeness, the total interior field can be expressed as a sum of the interior fields within each constituent, permitting the expansion

$$\theta(\mathbf{r}) \mathbf{E}_m(\mathbf{r}) = \sum_a \sum_\mu c_{m;a,\mu} \tilde{\theta}_a(\mathbf{r}) \tilde{\mathbf{E}}_{a,\mu}(\mathbf{r}), \quad (4)$$

where $c_{m;a,\mu}$ are weights yet to be found. These weights describe the relative contribution of the various single-particle modes to the cluster mode, thus potentially providing valuable physical insight. We restrict Eq. (1) to the interior of $\theta(\mathbf{r})$, which allows us to insert Eq. (4) to obtain

$$\begin{aligned} s_m \sum_a \sum_\mu c_{m;a,\mu} \tilde{\theta}_a(\mathbf{r}) \tilde{\mathbf{E}}_{a,\mu}(\mathbf{r}) \\ = k^2 \sum_a \sum_\mu c_{m;a,\mu} \int \bar{\bar{G}}_0(\mathbf{r}, \mathbf{r}') \tilde{\theta}_a(\mathbf{r}') \tilde{\mathbf{E}}_{a,\mu}(\mathbf{r}') d\mathbf{r}', \end{aligned} \quad (5)$$

which is simplified using the eigenvalue equation for the constituents (3) to give

$$s_m \sum_a \sum_\mu c_{m;a,\mu} \tilde{\theta}_a(\mathbf{r}) \tilde{\mathbf{E}}_{a,\mu}(\mathbf{r}) = \sum_a \sum_\mu c_{m;a,\mu} s_{a,\mu} \tilde{\mathbf{E}}_{a,\mu}(\mathbf{r}). \quad (6)$$

This step is possible because kernels of the integrals in Eqs. (1) and (3) are identical, corresponding to the free-space Green's tensor. The only difference between the two sides of Eq. (6) is that the LHS is valid only in the interiors, while the right-hand side is valid everywhere. Projection onto an adjoint mode $\tilde{\mathbf{E}}_{b,v}^\dagger$ then gives

$$\begin{aligned} s_m \sum_a \sum_\mu c_{m;a,\mu} \int \tilde{\mathbf{E}}_{b,v}^\dagger(\mathbf{r}) \tilde{\theta}_b(\mathbf{r}) \tilde{\theta}_a(\mathbf{r}) \tilde{\mathbf{E}}_{a,\mu}(\mathbf{r}) d\mathbf{r} \\ = \sum_a \sum_\mu c_{m;a,\mu} s_{a,\mu} \int \tilde{\mathbf{E}}_{b,v}^\dagger(\mathbf{r}) \tilde{\theta}_b(\mathbf{r}) \tilde{\mathbf{E}}_{a,\mu}(\mathbf{r}) d\mathbf{r}, \\ s_m c_{m;b,v} = \sum_a \sum_\mu V_{b,v;a,\mu} \tilde{s}_{a,\mu} c_{m;a,\mu}, \end{aligned} \quad (7)$$

where we have simplified the LHS using the orthogonality relation

$$\int \tilde{\mathbf{E}}_{b,v}^\dagger(\mathbf{r}) \tilde{\theta}_b(\mathbf{r}) \tilde{\theta}_a(\mathbf{r}) \tilde{\mathbf{E}}_{a,\mu}(\mathbf{r}) d\mathbf{r} = \delta_{ab} \delta_{\mu\nu}. \quad (8)$$

This states that modes belonging to different constituents are orthogonal by virtue of the disjoint $\tilde{\theta}$ functions, while the different modes belonging to the same inclusion are mutually orthogonal. In Eq. (7), we have also defined the overlap integrals

$$V_{b,v;a,\mu} = \int \tilde{\mathbf{E}}_{b,v}^\dagger(\mathbf{r}) \tilde{\theta}_b(\mathbf{r}) \tilde{\mathbf{E}}_{a,\mu}(\mathbf{r}) d\mathbf{r}, \quad (9)$$

which overlaps known modes of different constituents evaluated entirely within the bounds of constituent b . Physically speaking, the overlaps describe how a certain mode of one of the inclusions is scattered or perturbed by the other inclusions in the system. Finally, the linear eigenvalue equation (7) can be cast in matrix form to obtain the modes of the cluster,

$$s\mathbf{c} = \mathbf{V} \text{diag}(\tilde{s}_{a,\mu})\mathbf{c}, \quad (10)$$

which can be solved for the coefficients.

We emphasize that the system of equations (10) is *significantly smaller* than the corresponding system of equations that would arise if this problem were solved using, e.g., a finite-element approach. Indeed, the size of our equation set (10) is determined by the square of the number of modes that have a non-negligible contribution to the solution. It also scales as the square of the number of inclusions. For large systems this can be improved through use of sparsification techniques such as the fast multipole method, attaining linear scaling with the number of inclusions. Meanwhile, in a direct finite-element calculation [e.g., of the vector Helmholtz equation, the differential form of Eq. (1)], the number of equations that has to be solved is determined by the much higher number of mesh elements. This advantage will naturally be more significant as the number and/or size and/or acuteness of the geometrical features of scatterers in the cluster increases. This unique favorable scaling is expected to make GENOME more attractive for complex systems.

One final step exists after the coefficients $c_{m;a,\mu}$ in Eq. (4) are found. The expansion (4) is valid only inside the inclusions, so to extend this to the whole domain, we insert it back into the defining eigenvalue problem (1),

$$\begin{aligned} s_m \mathbf{E}_m(\mathbf{r}) &= k^2 \sum_a \sum_\mu c_{m;a,\mu} \int \bar{\bar{G}}_0(\mathbf{r}, \mathbf{r}') \tilde{\theta}_a(\mathbf{r}') \tilde{\mathbf{E}}_{a,\mu}(\mathbf{r}') d\mathbf{r}' \\ &= \sum_a \sum_\mu c_{m;a,\mu} s_{a,\mu} \tilde{\mathbf{E}}_{a,\mu}(\mathbf{r}), \end{aligned} \quad (11)$$

where the result was simplified using the constituent eigenvalue problem (3). We implemented this expansion (11), which is usually preferable to the expansion (4) even in the interior of the inclusion, since it often converges faster.

Finally, the Green's tensor can be obtained via GENOME [34], using the cluster modes just found,

$$\begin{aligned} \bar{\bar{G}}(\mathbf{r}, \mathbf{r}') &= \bar{\bar{G}}_0(|\mathbf{r} - \mathbf{r}'|) + \frac{1}{k^2} \sum_m \frac{\varepsilon_i - \varepsilon_b}{(\varepsilon_m - \varepsilon_i)(\varepsilon_m - \varepsilon_b)} \\ &\quad \mathbf{E}_m(\mathbf{r}) \otimes \mathbf{E}_m^\dagger(\mathbf{r}'), \end{aligned} \quad (12)$$

where ε_i is the permittivity of the inclusion, the eigenpermittivities $\varepsilon_m = \varepsilon_b(1 - s_m^{-1})$, and the adjoint mode is the mode itself,

$$\mathbf{E}_\mu^\dagger(\mathbf{r}) = \mathbf{E}_\mu(\mathbf{r}). \quad (13)$$

This simple adjoint holds true for all nondegenerate modes, so it is applicable to all modes employed in this paper, as ellipses are not sufficiently symmetric to produce degeneracies [72]. Two contributions are present in Eq. (12). First, $\bar{\bar{G}}_0(|\mathbf{r} - \mathbf{r}'|)$ is the Green's tensor of the homogeneous background in the absence of any scatterers. It has a known form for the vector Helmholtz equation in one, two, and three dimensions.

Second, the entire contribution due to the cluster is expressed as a sum over its eigenmodes. Its variation over source \mathbf{r}' and detector \mathbf{r} coordinates is separable, both expressed in terms of the spatial variation of the same set of modes. It is also in some sense diagonal since only a single summation index m exists. This simple form allows the variation of $\bar{\bar{G}}(\mathbf{r}, \mathbf{r}')$ to be mapped easily, including the derivative Purcell factor and RET rates.

III. RESULTS

To exemplify the method, we implement a nontrivial solution, solving the Purcell enhancement and the FRET of QEs near an ellipse dimer. The considered two-dimensional z -invariant structure is represented in Fig. 1(a): the two ellipses have the same dimensions, with semiaxes of $\lambda/4$ and $\lambda/8$, where λ is the wavelength. They are tilted by $\varphi_1 = 90^\circ$ and $\varphi_2 = 45^\circ$, except in the optimization discussion of Fig. 3 below, where φ_2 varies. For FRET rate calculations, the donor QE is modeled by a dipole \mathbf{d}_D and will vary in position, while the acceptor dipole \mathbf{d}_A is fixed in the gap center, at a distance of $\lambda/16$ from the ellipses. For Purcell enhancement calculations, only a donor dipole of varying position is considered.

We use COMSOL MULTIPHYSICS to compute the eigenpermittivity modes of one elliptical rod. The software's in-built eigenfrequency mode solver is adapted with a *trivial* substitution trick to allow the eigenfrequencies to be reinterpreted as eigenpermittivities ε_μ (see Ref. [34]); its implementation does not require any specialized knowledge, which is required for the implementation of quasinormal modes. More specifically, the rod permittivity is set to unity, and the background medium of permittivity ε_b is set to be dispersive, such that the wave number remains equal to $\sqrt{\varepsilon_b}k$ regardless of the COMSOL eigenfrequency. The system has a radius of 1.5λ and is enclosed within perfectly matched layers of 0.5λ thickness, and the mesh elements of the rod have a maximum size of $\lambda/100$. In this paper, we fix the wavelength at $\lambda = 670$ nm, leading to a permittivity of the silver rod of $\varepsilon_i = -20.8 + 0.43j$.

We implement the rigorous hybridization formula (11) in MATLAB [73], importing from COMSOL the modal electric field profiles $\mathbf{E}_\mu(\mathbf{r})$ and their corresponding eigenpermittivities ε_μ . We perform the integration on the mesh elements for the overlap integrals in matrix \mathbf{V} [Eq. (9)], and from the solution of the eigenvalue problem [Eq. (10)], we build the new basis of hybridized modes $\mathbf{E}_m(\mathbf{r})$ as defined by Eq. (11). The Green's tensor is then computed from Eq. (12).

The convergence of the method is illustrated in Fig. 1(b) for metallic silver rods. We employ a pseudo- L_2 norm for the relative difference of the imaginary part of the electric field components:

$$\Delta \text{Im}(E) = 10 \log_{10} \sqrt{\frac{\int \text{Im}(E_x - E_{x,\text{ref}})^2 + \text{Im}(E_y - E_{y,\text{ref}})^2 dA}{AN}}, \quad (14)$$

where the reference solution is a COMSOL direct simulation, i.e., the direct calculation of the response of the dipole \mathbf{d}_A with the dimer, A is the area of an integration domain including the dimer [in the case of Fig. 1(b), $\lambda = 670$ nm, and the area is 800×600 nm² and centered on the dipole position \mathbf{d}_A], and N is a normalization factor taken to be the square of the maximal

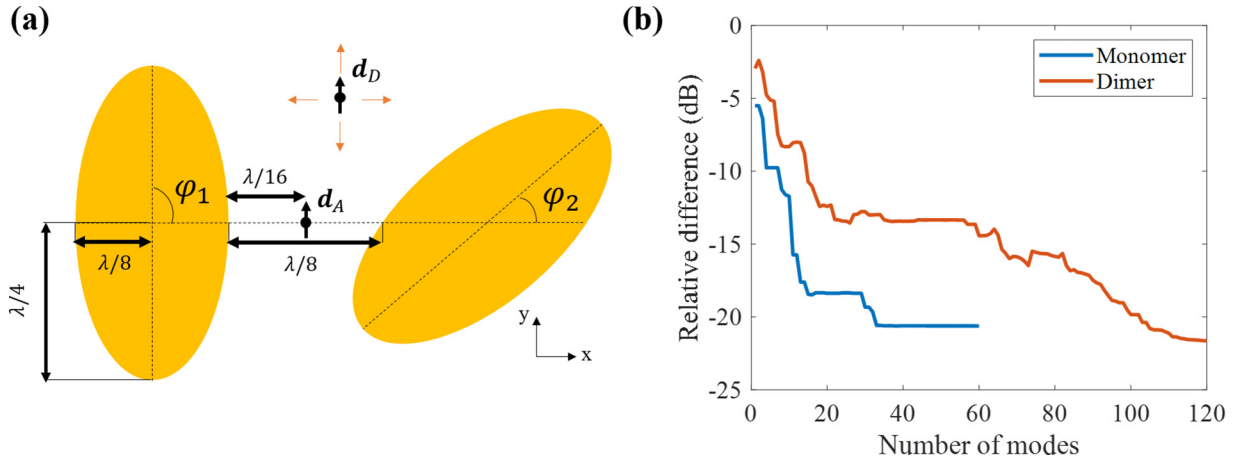


FIG. 1. Ellipse dimer considered and method convergence. (a) The y -oriented dipole \mathbf{d}_A is at the center of the gap in between the two ellipsoidal rods. In the case of FRET, the donor dipole \mathbf{d}_D varies position to generate the FRET map. The ellipses are tilted around their centers by $\varphi_1 = 90^\circ$ and $\varphi_2 = 45^\circ$ such that the gap size remains $\lambda/8$. (b) L_2 norm of the relative difference between direct simulations (COMSOL) and our mode expansion technique (GENOME), comparing the imaginary part of the electric field following Eq. (14). The monomer case is represented for comparison, resolving the geometry without the rod on the right.

value of the imaginary part of the field of the COMSOL solution. Note that $E_z = 0$ since we solve for the TM polarization.

In Fig. 1(b), good convergence is obtained after 20 modes for the elliptical monomer and saturates at -20 dB. This is due to numerical errors in the field discretization of the COMSOL direct simulation taken as the reference simulation and in the COMSOL mode generation constituting the building blocks of our Green's tensor. Moreover, we limit the mode search to 60 modes, truncating from the basis higher-order radial modes that would further enhance the accuracy. The constructed basis of the ellipse dimer expands on 120 modes, twice the number of modes of the monomer case, and Fig. 1(b) shows good convergence (-20 dB) after 90 modes. The number of modes required to obtain convergence, and therefore the computation time, depends on the permittivity of the rod, the inclination of the rod, the distance between the rods, and the position of the dipole. A quantitative study of this is beyond the scope of this paper, but heuristically, the field profiles of higher-order modes have more nodes and usually have a shorter extent into the background medium; therefore, their contribution to their overlap integral [Eq. (9)] is stronger for closer scatterers. The same reasoning applies for the distance of the source. Finally, the decay length depends on the local curvature of the ellipse, which explains the scatterers' relative orientation dependence.

The modes obtained from the hybridization formulation are now applied to compute the Purcell enhancement [Fig. 2(a)] and the FRET rate enhancement [Fig. 2(b)]. For direct simulations, we loop over the positions of the dipole \mathbf{d}_D , and we monitor the flux through a small box surrounding the dipole to compute the Purcell enhancement while measuring the field at the position of \mathbf{d}_A for the FRET rate enhancement. Although one direct simulation is fast, repeated simulation of varying emitter positions is time-consuming and can be prohibitive. With GENOME, the spatial dependence of the Green's tensor is constructed extremely rapidly from the knowledge of the spatial profile of the modes of the monomer, leading straightforwardly to the maps in Fig. 2. In order to illustrate the

speed of the method, we simulated the same problem with COMSOL and GENOME on the same computer (processor i7-6800K, 3.40 Ghz, 32 Gb RAM). It takes 11 min for the modes and 65 s to construct the matrix \mathbf{V} , solve the eigenvalue problem of the dimer structure, and retrieve the Purcell and FRET rate enhancement maps. Meanwhile, direct COMSOL simulations take 17 h, even though the mesh is coarser than for the GENOME mode calculation: the maximum element size within the rod is $\lambda/60$ for COMSOL and $\lambda/100$ for the mode search. Moreover, GENOME also gives access to the two other polarization directions in 2 s, while COMSOL needs another 17 h for each polarization. A complete complexity analysis deserves a separate study to formally define a limit where GENOME is faster. In addition, further speed improvements can be realized by exploiting symmetries in the matrix \mathbf{V} and with an implementation method that reduces the number of connections between COMSOL and MATLAB. Note that maps of FRET enhancement computed via direct simulations can be fast when one emitter (donor or acceptor) is fixed, thanks to the property $G_{ij}(\mathbf{r}_D, \mathbf{r}_A, \omega) = G_{ji}(\mathbf{r}_A, \mathbf{r}_D, \omega)$ of the Green's tensor. For results where neither emitter is fixed, GENOME is faster.

The Purcell enhancement Γ_e is given by

$$\Gamma_e = \frac{\mathbf{d}_D^* \cdot \text{Im}[\bar{\bar{\mathbf{G}}}(\mathbf{r}_D, \mathbf{r}_D, \omega_0)] \cdot \mathbf{d}_D}{\mathbf{d}_D^* \cdot \text{Im}[\bar{\bar{\mathbf{G}}}_0(\mathbf{r}_D, \mathbf{r}_D, \omega_0)] \cdot \mathbf{d}_D}. \quad (15)$$

It is represented in Fig. 2(a) for all positions of a y -polarized dipole outside the dimer, with the interior of the dimer represented in black. The strongest Purcell enhancement, exceeding $\Gamma_e = 6$, is observed for a dipole close to the tips of the ellipses. In Fig. 2(c), we compare the GENOME formulation to COMSOL direct simulations: we use the metric defined in Eq. (14), where we replace the electric field by the Purcell enhancement or the FRET rate enhancement. In general, a great accuracy of -40 dB is obtained, except for a small region of 5 nm around the edges of the ellipses, where the accuracy is above -20 dB. This indicates missing

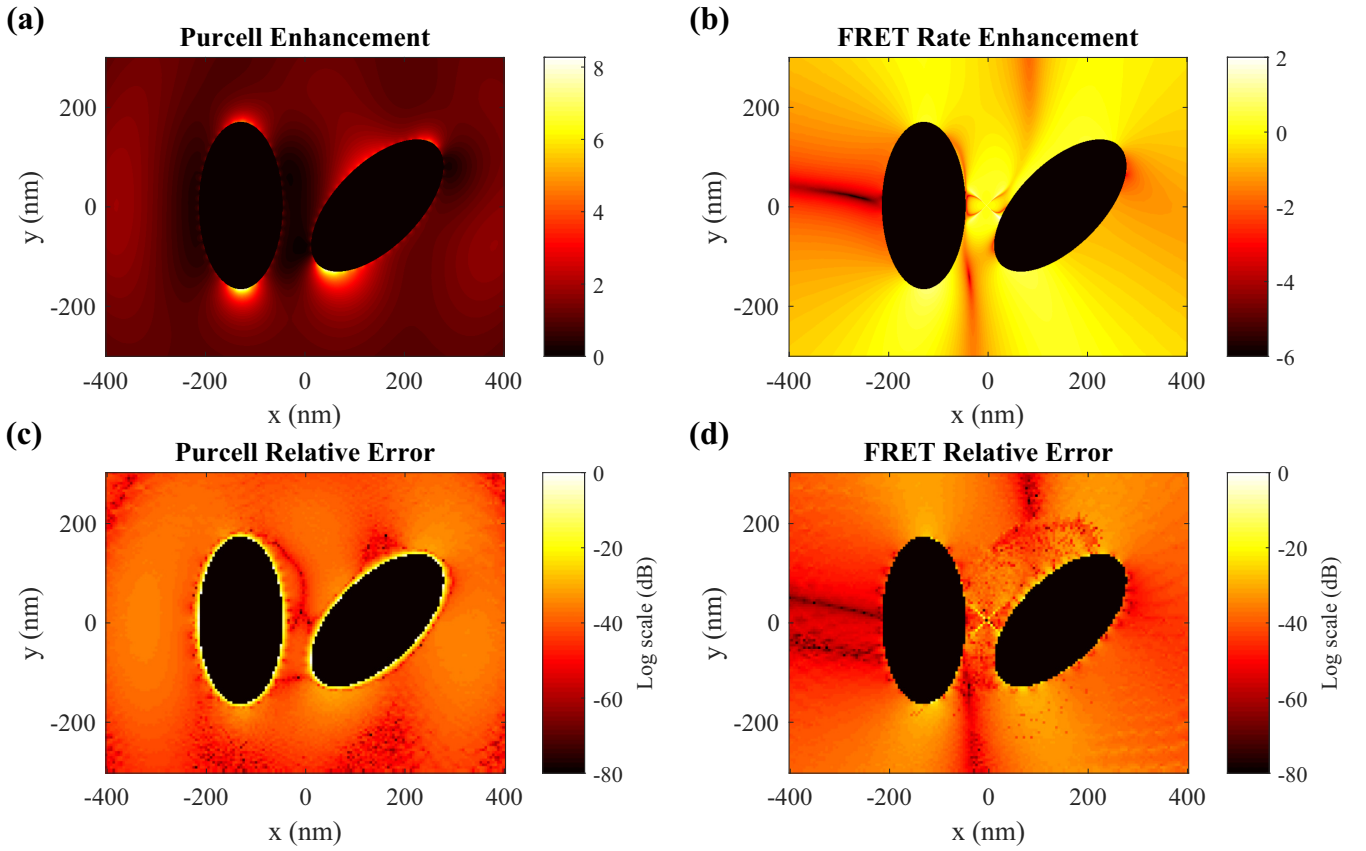


FIG. 2. Efficient mapping of Purcell and FRET rate enhancement. The geometry of Fig. 1(a) is resolved for (a) the Purcell enhancement and (b) the FRET rate enhancement. The L_2 norm of the relative difference from COMSOL simulations is represented for (c) the Purcell enhancement and (d) the FRET rate enhancement. This degree of convergence (mean error is -40 dB for both maps) is obtained for 50 monomer modes. The map generation takes 11 min for the mode calculation and an additional 65 s for the hybridization method (with room for improvement), while COMSOL takes 17 h.

higher-order ultraconfined plasmonic modes in the expansion. This inaccuracy can be addressed by considering more modes in the expansion, if it is necessary for the region of interest. Note, however, that at those distances quantum corrections may be required: the point-dipole approximation is no longer valid for the QE [74], and nonlocal effects cannot be neglected very close to the particle [75].

The FRET rate enhancement is computed for the same dimer in Fig. 2(b) for all positions of the y -polarized donor outside the dimer, where the acceptor is in the center of the gap. The FRET rate enhancement Γ_{DA} is given by [6,14]

$$\Gamma_{DA} = \frac{|\mathbf{d}_A^* \cdot \bar{\mathbf{G}}(\mathbf{r}_A, \mathbf{r}_D, \omega_0) \cdot \mathbf{d}_D|^2}{|\mathbf{d}_A^* \cdot \bar{\mathbf{G}}_0(\mathbf{r}_A, \mathbf{r}_D, \omega_0) \cdot \mathbf{d}_D|^2}, \quad (16)$$

where we suppose that the donor and acceptor absorption spectra in free space are identical and are equal to a δ function centered on ω_0 . The strongest enhancements appear when the donor is close to the acceptor but also around the tips of the ellipses. On the contrary, the FRET rate enhancement is inhibited for a donor positioned on the left of the dimer. Comparing the Purcell enhancement and the FRET rate [Figs. 2(a) and 2(b)] shows that the FRET rate and the imaginary part of the Green's tensor [i.e., Purcell, see Eq. (15)] are uncorrelated, as demonstrated in Ref. [15], closing the ongoing debate on the

influence of the imaginary part of the Green's tensor (related to the local density of states) at the position of the donor on the FRET rate. The comparison with direct simulations is represented in Fig. 2(d), using an L_2 norm similar to Eq. (14). In general, we reach an excellent agreement of -40 dB, with particular zones around the edges of the ellipses amounting to a larger error of -20 dB, which we relate to the missing higher-order plasmonic modes in the expansion.

Our method is powerful for applications relying on the spatial variation of the Green's tensor. Indeed, once the new mode basis of the hybridized mode is known, $\bar{\mathbf{G}}(\mathbf{r}, \mathbf{r}', \omega_0)$ is determined over the entire space, hence allowing for diverse optimizations. In Fig. 3, we optimize the Purcell enhancement as a function of the ellipse rotation ($\varphi_1 = 90^\circ$ and φ_2 varies), dipole orientation, and dipole location along the vertical line $x = 0$. Note that the ellipse is rotated such that the gap size remains $\lambda/8$ at $y = 0$. The blue line shows an optimum for an ellipse tilted by $\varphi_2 = 38^\circ$ and an x -oriented dipole at position $y = -78$ nm. The real part of the corresponding electric field (x component) is represented in inset (1), showing that the maximum Purcell enhancement is obtained for a geometry where the dipole is the closest to the right rod. A local maximum of 5.5 is reached for parallel ellipses (tilted by $\varphi_1 = \varphi_2 = 90^\circ$) and an x -oriented dipole at position $y = 0$ nm, with the field represented in (2). The orange and yellow curves are

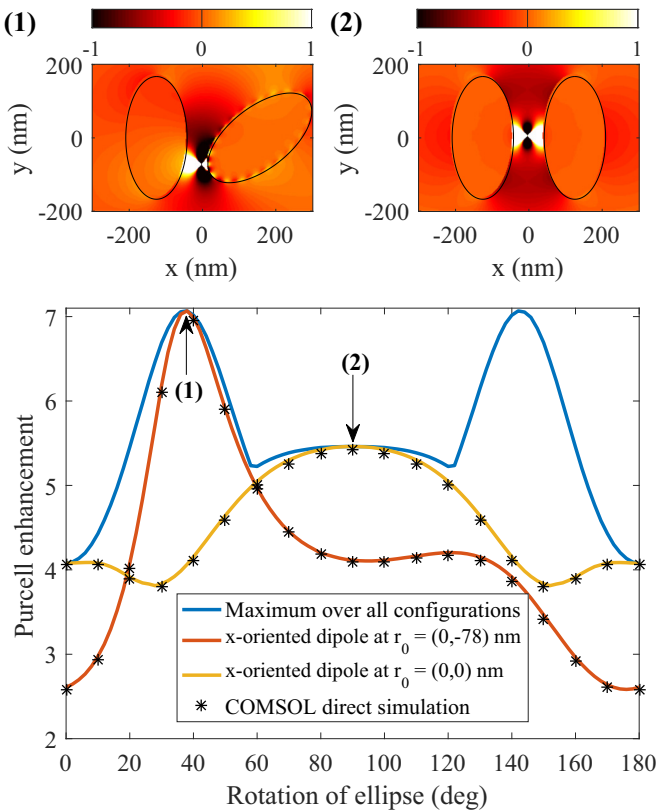


FIG. 3. Maximum Purcell enhancement over the ellipse rotation φ_2 , the dipole position along line $x = 0$, and the dipole orientation. The blue line represents the maximum of the Purcell enhancement computed comparing all dipole orientations (181 points) and positions (301 points). The orange line represents the x -oriented dipole at $y = -78$ nm, reaching a maximum for an ellipse titled by $\varphi_2 = 38^\circ$. The yellow line represents the same dipole at $y = 0$. The black asterisks are COMSOL direct simulations, in excellent agreement with our hybridization method. The real part of the normalized x component of the electric field is plotted above for the two maxima, (1) and (2).

plotted for specific dipole orientations and locations, showing excellent agreement with COMSOL direct simulations (black asterisks). The maximum appearing at $\varphi_2 = 142^\circ$ is due to the situation symmetric to the orange curve, with an x -oriented dipole at position $y = 78$ nm. In this particular example, 5×10^6 configurations (91 ellipse rotations, 301 dipole positions, and 181 orientations) were computed in 19 min (with the modes already known), i.e., 1000 times faster than direct simulations (3 s per configuration).

IV. SUMMARY

In this paper, we implemented an electrodynamic formulation of eigenpermittivity mode hybridization, retrieving the Green's tensor of a dimer of scatterers from the eigenpermittivity modes of the constituent scatterers. The method gives quick access to complete spatial maps of the FRET rate and Purcell enhancements normalized to free-space rates for different positions of the source. The maps show regions of inhibited and amplified rates, and their comparison

demonstrates that, although similar, they differ at some positions of the source. It indicates that the FRET rate cannot be optimized only through the imaginary part of the Green's function, i.e., the local density of states [14,15], as is sometimes the case.

The formulation was successfully tested for an ellipse dimer, and the implementation for more scatterers of general and nonidentical shapes is straightforward. As we discussed, these calculations generalize previous works beyond the quasistatic approximation [42,64]; they also constitute a rigorous generalization of the approximate hybridization technique developed independently later by Prodan, Nordlander, and coworkers (e.g., Refs. [70,71]), which applied a microscopic, physically intuitive model of a quasi-free-electron gas to derive the complex eigenfrequencies of various complicated plasmonic nanostructures. Indeed, our approach does not rely on assumptions such as the negligibility of the valence band electrons, the incompressibility of the electron cloud, the absence of Drude losses and of interband transitions, or the jellium approximation of the ion background; in contrast, our approach accounts for absorption losses in addition to and independently of radiation losses, thus, capturing the open and lossy nature of these systems. Finally, our calculations can be used to validate various analytic approaches already applied to the problem of particle dimers in the case of transformation optics [76] and also to even more complicated structures [77–79]. Moreover, for physical phenomena arising from interference between several modes, GENOME can provide information on the modes and hybridization at play and lead to an efficient optimization route. This is, for example, relevant in the context of Fano resonances [77,78], which are the result of the interference between a background and a resonant mode, or in the context of plasmon-induced transparency [79], which is the result of the interaction between a dark mode and a radiative mode.

The method is in good agreement with direct simulations and is orders of magnitude faster, even including the time required to find modes of a single particle. It is therefore suitable for applications requiring the spatial variation of the Green's tensor, as we show for maps of Purcell and FRET rate enhancement. We also envision it to play a major role in quantum computation, particularly in quantum plasmonics, to quantify the high-order decay rates of quantum emitters [74], for free-electron high-harmonic light sources [80,81], heat transfer and thermal emission engineering [82–85], van der Waals forces [86], and disordered media [87]. For simple systems, the method also allows for greater physical insight into the interactions among the constituents as it is a weighted sum of constituent modes of the single particle. Further work is underway to generalize the method to periodic structures, to three-dimensional particles, to nonuniform permittivities [88], and to anisotropic media to ensure that GENOME benefits a wide range of research fields.

ACKNOWLEDGMENTS

G.R. was supported by the Fonds De La Recherche Scientifique - FNRS (Research project T.0166.20 and Grant FC 95592). P.Y.C. and Y.S. acknowledge support from the Israel Science Foundation (ISF) (Grant No. 899/16).

- [1] E. M. Purcell, *Phys. Rev.* **69**, 37 (1946).
- [2] L. Novotny and B. Hecht, *Principles of Nano-optics* (Cambridge University Press, Cambridge, 2006).
- [3] A. F. Koenderink, *ACS Photonics* **4**, 710 (2017).
- [4] A. Dousse, J. Suffczynski, A. Beveratos, O. Krebs, A. Lemaître, I. Sagnes, J. Bloch, P. Voisin, and P. Senellart, *Nature (London)* **466**, 217 (2010).
- [5] S. I. Maslovski and C. R. Simovski, *Nanophotonics* **8**, 429 (2019).
- [6] H. T. Dung, L. Knöll, and D.-G. Welsch, *Phys. Rev. A* **65**, 043813 (2002).
- [7] P. Andrew, *Science* **290**, 785 (2000).
- [8] C. E. Finlayson, D. S. Ginger, and N. C. Greenham, *Chem. Phys. Lett.* **338**, 83 (2001).
- [9] P. Ghenuche, J. de Torres, S. B. Moparthi, V. Grigoriev, and J. Wenger, *Nano Lett.* **14**, 4707 (2014).
- [10] J. Ren, T. Wu, B. Yang, and X. Zhang, *Phys. Rev. B* **94**, 125416 (2016).
- [11] F. Reil, U. Hohenester, J. R. Krenn, and A. Leitner, *Nano Lett.* **8**, 4128 (2008).
- [12] L. Zhao, T. Ming, L. Shao, H. Chen, and J. Wang, *J. Phys. Chem. C* **116**, 8287 (2012).
- [13] K.-S. Kim, J.-H. Kim, H. Kim, F. Laquai, E. Arifin, J.-K. Lee, S. I. Yoo, and B.-H. Sohn, *ACS Nano* **6**, 5051 (2012).
- [14] M. Wubs and W. L. Vos, *New J. Phys.* **18**, 053037 (2016).
- [15] C. L. Cortes and Z. Jacob, *Opt. Express* **26**, 19371 (2018).
- [16] A. Salam, *Atoms* **6**, 56 (2018).
- [17] G. A. Jones and D. S. Bradshaw, *Front. Phys.* **7**, 100 (2019).
- [18] E. A. Jares-Erijman and T. M. Jovin, *Nat. Biotechnol.* **21**, 1387 (2003).
- [19] I. L. Medintz, A. R. Clapp, H. Mattoussi, E. R. Goldman, B. Fisher, and J. M. Mauro, *Nat. Mater.* **2**, 630 (2003).
- [20] G. K. Mor, J. Basham, M. Paulose, S. Kim, O. K. Varghese, A. Vaish, S. Yoriya, and C. A. Grimes, *Nano Lett.* **10**, 2387 (2010).
- [21] S.-A. Biehs and G. S. Agarwal, *Appl. Phys. Lett.* **103**, 243112 (2013).
- [22] K. N. Avanaki, W. Ding, and G. C. Schatz, *J. Phys. Chem. C* **122**, 29445 (2018).
- [23] J. R. Zurita-Sánchez and J. Méndez-Villanueva, *Plasmonics* **13**, 873 (2017).
- [24] L.-Y. Hsu, W. Ding, and G. C. Schatz, *J. Phys. Chem. Lett.* **8**, 2357 (2017).
- [25] A. V. Lavrinenko, J. Lægsgaard, N. Gregersen, F. Schmidt, and T. Søndergaard, *Numerical Methods in Photonics* (CRC Press, Boca Raton, FL, 2018).
- [26] A. Agrawal, T. Benson, R. M. D. L. Rue, and G. A. Wurtz, *Recent Trends in Computational Photonics*, Springer Series in Optical Sciences Vol. 204 (Springer, NYC, 2017).
- [27] A. Taflove, A. Oskooi, and S. G. Johnson, *Advances in FDTD Computational Electrodynamics: Photonics and Nanotechnology*, Artech House Antennas and Propagation Library (Artech House, Norwood, Massachusetts, 2013).
- [28] C. Sauvan, J. P. Hugonin, I. S. Maksymov, and P. Lalanne, *Phys. Rev. Lett.* **110**, 237401 (2013).
- [29] M. B. Doost, W. Langbein, and E. A. Muljarov, *Phys. Rev. A* **90**, 013834 (2014).
- [30] R.-C. Ge, P. T. Kristensen, J. F. Young, and S. Hughes, *New J. Phys.* **16**, 113048 (2014).
- [31] T. Weiss, M. Mesch, M. Schäferling, H. Giessen, W. Langbein, and E. A. Muljarov, *Phys. Rev. Lett.* **116**, 237401 (2016).
- [32] S. Franke, S. Hughes, M. K. Dezfouli, P. T. Kristensen, K. Busch, A. Knorr, and M. Richter, *Phys. Rev. Lett.* **122**, 213901 (2019).
- [33] F. Alpeggiani, N. Parappurath, E. Verhagen, and L. Kuipers, *Phys. Rev. X* **7**, 021035 (2017).
- [34] P. Y. Chen, D. J. Bergman, and Y. Sivan, *Phys. Rev. Appl.* **11**, 044018 (2019).
- [35] P. Lalanne, W. Yan, K. Vynck, C. Sauvan, and J.-P. Hugonin, *Laser Photonics Rev.* **12**, 1700113 (2018).
- [36] E. A. Muljarov and W. Langbein, *Phys. Rev. B* **93**, 075417 (2016).
- [37] E. A. Muljarov, W. Langbein, and R. Zimmermann, *Europhys. Lett.* **92**, 50010 (2011).
- [38] W. Yan, R. Faggiani, and P. Lalanne, *Phys. Rev. B* **97**, 205422 (2018).
- [39] T. Weiss, M. Schäferling, H. Giessen, N. A. Gippius, S. G. Tikhodeev, W. Langbein, and E. A. Muljarov, *Phys. Rev. B* **96**, 045129 (2017).
- [40] D. J. Bergman and D. Stroud, *Phys. Rev. B* **22**, 3527 (1980).
- [41] M. S. Agranovich, B. Z. Katsenelenbaum, A. N. Sivov, and N. N. Voitovich, *Generalized Method of Eigenoscillations in Diffraction Theory* (Wiley-VCH, Weinheim, 1999).
- [42] D. J. Bergman, *Phys. Rev. B* **19**, 2359 (1979).
- [43] T. Sandu, *Plasmonics* **8**, 391 (2013).
- [44] D. J. Bergman, *J. Phys. C* **12**, 4947 (1979).
- [45] D. J. Bergman and K.-J. Dunn, *Phys. Rev. B* **45**, 13262 (1992).
- [46] O. D. Miller, A. G. Polimeridis, M. T. H. Reid, C. W. Hsu, B. G. DeLacy, J. D. Joannopoulos, M. Soljačić, and S. G. Johnson, *Opt. Express* **24**, 3329 (2016).
- [47] D. J. Bergman and M. I. Stockman, *Phys. Rev. Lett.* **90**, 027402 (2003).
- [48] K. Li, M. I. Stockman, and D. J. Bergman, *Phys. Rev. Lett.* **91**, 227402 (2003).
- [49] M. I. Stockman, D. J. Bergman, C. Anceau, S. Brasselet, and J. Zyss, *Phys. Rev. Lett.* **92**, 057402 (2004).
- [50] M. I. Stockman, S. V. Faleev, and D. J. Bergman, *Phys. Rev. Lett.* **88**, 067402 (2002).
- [51] K. Li, M. I. Stockman, and D. J. Bergman, *Phys. Rev. B* **72**, 153401 (2005).
- [52] K. N. Reddy, P. Y. Chen, A. I. Fernández-Domínguez, and Y. Sivan, *J. Opt. Soc. Am. B* **34**, 1824 (2017).
- [53] A. Farhi and D. J. Bergman, *Phys. Rev. A* **90**, 013806 (2014).
- [54] O. Schnitzer, V. Giannini, S. A. Maier, and R. V. Craster, *Proc. R. Soc. A* **472**, 20160258 (2016).
- [55] O. Schnitzer, *IMA J. Appl. Math.* **84** 813 (2019).
- [56] A. Farhi and D. J. Bergman, *Phys. Rev. A* **93**, 063844 (2016).
- [57] C. Forestiere and G. Miano, *Phys. Rev. B* **94**, 201406(R) (2016).
- [58] M. Pascale, G. Miano, and C. Forestiere, *J. Opt. Soc. Am. B* **34**, 1524 (2017).
- [59] P. Y. Chen and Y. Sivan, *Comput. Phys. Commun.* **214**, 105 (2017).
- [60] T. Hoehne, L. Zschiedrich, N. Haghghi, J. A. Lott, and S. Burger, *Proc. SPIE* **10682**, 106821U (2018).
- [61] L. Ge, Y. D. Chong, and A. D. Stone, *Phys. Rev. A* **82**, 063824 (2010).

- [62] C. Forestiere, G. Miano, G. Rubinacci, A. Tamburrino, R. Tricarico, and S. Ventre, *IEEE Trans. Antennas Propag.* **66**, 2505 (2018).
- [63] J. Huheey, *Inorganic Chemistry: Principles of Structure and Reactivity*, 4th ed. (Prentice Hall, Upper Saddle River, New Jersey, 1972).
- [64] J. I. Gersten and A. Nitzan, *Surf. Sci.* **158**, 165 (1985).
- [65] N. Liver, A. Nitzan, and K. F. Freed, *J. Chem. Phys.* **82**, 3831 (1985).
- [66] N. Liver, A. Nitzan, and J. Gersten, *Chem. Phys. Lett.* **111**, 449 (1984).
- [67] M. Pascale, G. Miano, R. Tricarico, and C. Forestiere, *Sci. Rep.* **9** 14524 (2019).
- [68] X. Wang, X.-G. Zhang, Q. Yu, and B. N. Harmon, *Phys. Rev. B* **47**, 4161 (1993).
- [69] P. Chen, M. Byrne, A. Asatryan, L. Botten, K. Dossou, A. Tuniz, R. McPhedran, C. De Sterke, C. Poulton, and M. Steel, *Waves Random Complex Media* **22**, 531 (2012).
- [70] E. Prodan, C. Radloff, N. J. Halas, and P. Nordlander, *Science* **302**, 419 (2003).
- [71] P. Nordlander, C. Oubre, E. Prodan, K. Li, and M. I. Stockman, *Science* **4**, 899 (2004).
- [72] In cases where degeneracies are present, (13) still holds if the degenerate pairs are chosen appropriately. For example, if there is continuous rotational symmetry along an angle ϑ , then basis modes with $\sin(m\vartheta)$ and $\cos(m\vartheta)$ variation satisfy (13), but modes with $e^{im\vartheta}$ require a modified form of (13).
- [73] Code available at www.umons.ac.be/nanophot.
- [74] N. Rivera, I. Kaminer, B. Zhen, J. D. Joannopoulos, and M. Soljačić, *Science* **353**, 263 (2016).
- [75] E. Castanić, M. Boffety, and R. Carminati, *Opt. Lett.* **35**, 291 (2010).
- [76] A. Aubry, D. Lei, S. A. Maier, and J. B. Pendry, *ACS Nano* **5**, 3293 (2011).
- [77] V. Giannini, Y. Francescato, H. Amrania, C. C. Phillips, and S. A. Maier, *Nano Lett.* **11**, 2835 (2011).
- [78] M. Hentschel, D. Dregely, R. Vogelgesang, H. Giessen, and N. Liu, *ACS Nano* **5**, 2042 (2011).
- [79] S. Zhang, D. A. Genov, Y. Wang, M. Liu, and X. Zhang, *Phys. Rev. Lett.* **101**, 047401 (2008).
- [80] N. Rivera, L. J. Wong, M. Soljačić, and I. Kaminer, *Phys. Rev. Lett.* **122**, 053901 (2019).
- [81] G. Rosolen, L. J. Wong, N. Rivera, B. Maes, M. Soljačić, and I. Kaminer, *Light: Sci. Appl.* **7**, 64 (2018).
- [82] Y. Guo and Z. Jacob, *Opt. Express* **21**, 15014 (2013).
- [83] Y. Guo, S. Molesky, H. Hu, C. L. Cortes, and Z. Jacob, *Appl. Phys. Lett.* **105**, 073903 (2014).
- [84] M. Francoeur, M. P. Mengüç, and R. Vaillon, *J. Quant. Spectrosc. Radiat. Transfer* **110**, 2002 (2009).
- [85] B. Czaplá and A. Narayanaswamy, *Phys. Rev. B* **96**, 125404 (2017).
- [86] Y. Luo, R. Zhao, and J. B. Pendry, *Proc. Natl. Acad. Sci. USA* **111**, 18422 (2014).
- [87] A. P. Mosk, A. Lagendijk, G. Lerosey, and M. Fink, *Nat. Photonics* **6**, 283 (2012).
- [88] P. Y. Chen, Y. Sivan, and E. A. Muljarov, [arXiv:2002.01784](https://arxiv.org/abs/2002.01784).